PAPER • **OPEN ACCESS**

Digitally controlled mechatronic metamaterials for actively induced targeted bandgaps

To cite this article: Vivek Gupta *et al* 2026 *Smart Mater. Struct.* **35** 085026

IOP Publishing Smart Mater. Struct. 35 (2026) 085026 https://doi.org/10.1088/1361-665X/ae92c3

Smart Materials and Structures

OPEN ACCESS

RECEIVED
14 March 2026

REVISED
1 July 2026

ACCEPTED FOR PUBLICATION
30 July 2026

PUBLISHED
17 August 2026

PAPER

Digitally controlled mechatronic metamaterials for actively induced targeted bandgaps

Vivek Gupta*, Aditya Natu and S Hassan HosseinNia

Delft University of Technology, Delft, The Netherlands

* Author to whom any correspondence should be addressed.

E-mail: v.gupta-2@tudelft.nl, viv02feb1990@gmail.com, A.M.Natu@tudelft.nl and S.H.HosseinNiaKani@tudelft.nl

Keywords: metamaterial, metastructure, second-order low-pass, programmable, bandgaps, feedback controller

Abstract

Passive elastic metamaterials offer effective vibration attenuation through locally resonant bandgaps, but suffer from fundamental limitations in real-time tunability, narrow operational bandwidth, and non-adaptive behavior. This work presents an experimental framework for inducing and tuning vibration bandgaps in digitally controlled mechatronic metamaterials. A slender-beam structure instrumented with collocated piezoelectric sensor–actuator pairs distributed periodically along the length is used as the host medium, with decentralized second-order low-pass resonant filter with negative position feedback controllers implemented in real time on an FPGA platform. Unlike conventional approaches that assess bandgap formation through lateral tip displacement, this study motivates the choice of bandgap indicator through bending strain minimization at the piezoelectric sensors, and validates bandgap formation quantitatively through end-to-end closed-loop transmissibility. This more accurately reflects the moment-based phase cancellation dynamics underlying resonant actuation. Closed-form analytical expressions for transmissibility in a general $n \times n$ decentralized feedback architecture are derived via block elimination and experimentally validated using the 7×7 unit-cell configuration. The results demonstrate that targeted low-frequency bandgaps in the range of 20–100 Hz can be systematically induced and reshaped through programmable tuning of controller gain and damping ratio, significantly improving vibration attenuation. By shifting the focus to localized dynamics, this work deepens the understanding of how control-induced bandgaps emerge and demonstrates a scalable pathway for designing programmable mechatronic metamaterials based on digitally synthesized resonator dynamics.

1. Introduction

The growing demand for nanometer-level motion accuracy in high-precision mechatronic systems has created an urgent need for compact and tunable vibration suppression strategies capable of operating under varying dynamic conditions. The engineering of elastic and acoustic metamaterials has seen major advances in recent years, with increased emphasis on actively tunable systems that can adapt to changing environments or performance criteria, e.g. Liu *et al* (2000), Hussein *et al* (2014), Sugino *et al* (2017), Failla *et al* (2024). Such designed metamaterials with locally resonant units provide the basis for bandgap formation, enabling the suppression of vibrations and elastic waves within specific frequency ranges (Sugino *et al* 2016, Gupta *et al* 2020, 2022). However, conventional passive implementations face limitations in real-time tunability, narrow bandwidth, and non-adaptive behavior, particularly in scenarios demanding dynamic control. To overcome these constraints, research has increasingly focused on digitally controlled mechatronic metamaterials that make use of embedded sensors, actuators (e.g. piezoelectrics), and feedback algorithms for active wave manipulation.

A notable research trajectory involves integrating piezoelectric transducers with digital feedback control to form programmable unit cells capable of altering their local stiffness and damping characteristics in real time, as demonstrated in recent studies. For example, (Fang *et al* 2022) and (Yuan *et al* 2019) developed programmable acoustic lattices by synchronizing piezoelectric resonators with digital controllers to create wide and shiftable bandgaps. Lin and Tol (2023) explored tunable phononic crystals with embedded piezo-patches for real-time vibration filtering through metasurfaces with resonant piezoelectric shunts. Nima Mahmoodi *et al* (2010) employed second-order low-pass resonant filters with negative position feedback and adaptive gain strategies to precisely control the onset and width of stopbands.

Across many existing works, the analytical modeling of piezoelectric beam structures has advanced our understanding of tunable bandgaps for vibration control. Huang and Sun (2009) derived dispersion relations in rods with shunted piezo patches, while (Hussein *et al* 2014) formalized phononic wave modeling in periodic media. Das *et al* (2025) provided exact solutions for sandwich beams with periodic piezo elements. Kaczmarek *et al* (2024a, 2024b)integrated active control into beam bandgap analysis, and Zhu *et al* (2014) offered an effective medium framework for subwavelength wave behavior. However, the experimental validation of bandgap dynamics based on these analytical models remains largely unexplored, a gap that this work aims to address.

Several studies explored design changes to the host structure. For example, (Wen *et al* 2020) showed that a periodic variable cross-section design for the acoustic metamaterial beam is an effective measure to obtain wider and more numerous bandgaps, by coupling Bragg scattering with locally resonant bandgap mechanisms to enhance vibration reduction capacity over wide frequency ranges. Wu *et al* (2022) developed a metamaterial beam with high specific energy absorption coefficient using variable cross section. Their model optimized equal-section beam to the variable section using chained beam constraint model and the improvement in specific energy absorption is observed with variable section of the beam. Sugino *et al* (2016) investigated a metastructure consisting of a beam substrate with a periodic arrangement of spring-mass resonators. They showed the formation of a bandgap centered around the resonant frequency of the system, with the bandgap width being influenced by the ratio of the resonator mass to the mass of the beam segment corresponding to each unit cell. Similarly, (Huang *et al* 2016) examined a beam incorporating more complex resonators, consisting of inclined trusses integrated with conventional spring-mass resonators. Despite the increased complexity, the bandgaps were still observed near the natural frequencies of the spring-mass system.

While recent studies, such as Kaczmarek and HosseinNia (2024), have made important progress in demonstrating digitally controlled elastic metamaterials using the positive position feedback in finite beams, several aspects remain unexplored. Their work employs infinite-transducer approximations for analytical predictions, relies on tip displacement accelerometer data, and does not consider a periodic unit-cell-based metamaterial beam for experimental validation. The present work advances the state of the art along four distinct and previously unaddressed axes:

First, we derive a closed-form transmissibility expression for a finite $n \times n$ decentralized negative feedback architecture via block matrix elimination, without invoking the infinite-transducer approximation. This yields an analytically compact and experimentally verifiable prediction for end-to-end vibration transmissibility in a controlled metabeam of arbitrary size.

Second, we motivate the choice of bandgap indicator through bending strain minimization at the collocated piezoelectric sensors. This perspective directly reflects the moment-based phase cancellation dynamics of resonant actuation and provides physical insight into the unit-cell-level origin of control-induced bandgaps. Bandgap formation is then quantitatively validated through end-to-end closed-loop transmissibility, which serves as the experimental metric throughout the study.

Third, the complete decentralized $7{\times}7$ feedback architecture is implemented in real time on an FPGA platform, demonstrating programmable and frequency-selective bandgap induction with systematic tunability through gain and damping adjustment across the 20–100 Hz range.

Fourth, we identify the RC high-pass characteristics of the charge amplifier circuit as a practical design consideration for low-frequency bandgap formation. We show that compensating for this parasitic signal attenuation through increased controller gain enables bandgap formation to be extended to low frequencies where passive methods are fundamentally limited.

This work experimentally demonstrates that bandgaps emerge at the scale of individual unit cells, and reveals how resonant control dynamics at that level translate into system-wide attenuation. This is a step closer to addressing the fundamental question of how resonant feedback can actively induce and tune targeted bandgaps, which has not yet been reported experimentally.

The remainder of this paper is organized as follows. Section 2 presents the experimental modeling framework, beginning with the architecture of the mechatronic metamaterials, details of the structure and hardware, and the controller implementation. This is followed by an analytical framework for the $n \times n$ feedback design, including derivations of the transmissibility ratio and an experimental case study on a 7×7 unit cell. Section 3 reports the experimental results and the observed bandgaps, with

Table 1. Comparison of the present work with representative state-of-the-art studies.

References	Structure	Units	Control	Freq. (Hz)	Metric	Platform
(Sugino et al 2016)	Cantilever beam	Periodic	Passive spring–mass	Resonance	Tip disp.	Analytical
(Kaczmarek et al 2024a)	Cantilever beam	4	PPF decentralized	10–320	Tip acc.	FPGA
(Yuan et al 2019)	Metastructure beam	5–10	Proportional feedback	100–500	Tip disp.	Digital
(Lin and Tol 2023)	Metasurface beam	Periodic	Resonant shunt	Tunable	Wavefront	Analogue
(Nima Mahmoodi et al 2010)	Flexible beam	Single	Adaptive PPF	Resonance	Tip disp.	Digital
(Das et al 2025)	Sandwich metabeam	Periodic	Piezo shunt	Analytical	Dispersion	Analytical
Present work	**Cantilever beam**	**7**	**2nd-order LP, $n \times n$**	**20–100**	**Bending**	**FPGA**

emphasis on the influence of controller gains and damping. Section 4 provides a broader discussion of the findings, and section 5 concludes the paper with final remarks and outlook.

To clearly position the contributions of the present work, table 1 provides a quantitative comparison with representative state-of-the-art studies on active piezoelectric metastructures and digitally controlled metamaterials.

2. Experimental modeling of bandgaps through mechatronic approach

This section introduces the structure and simplified model of the active piezoelectric metamaterial beam, followed by an overview of the control architecture and implemented controllers. Finally, algebraic expressions are derived to demonstrate the targeted and enhanced bandgaps achieved through different control strategies. Schematic representation of a single unit cell integrated with a collocated actuator–sensor with the representation of a metabeam with the jth unit cells distributed along its length is shown in figure 1.

2.1. Structure and hardware

The experimental setup of the studied structure consists of a slender aluminum alloy beam, assumed in simulations with a density of $\rho_s = 2700\,\mathrm{kg\,m^{-3}}$ and an elastic modulus of $C_s = 69\,\mathrm{GPa}$. The beam is rigidly clamped at its base using the fixtures, as shown in figure 2. The vibrational response at both the tip and the clamped base of the beam is captured using accelerometers, whose signals are subsequently processed to determine the system transmissibility and evaluate performance.

Collocated piezoelectric patch actuators and sensors (PI P-876.SP1 DuraAct) are mounted on the beam, with seven sensor–actuator pairs implemented to generate the desired bandgaps. The piezo patches serve in both actuation and sensing roles. Signal conditioning is carried out using custom-built charge amplifiers based on TL074 operational amplifiers. The resulting transfer function between the piezoelectric sensor charge and the amplifier voltage output is expressed as

$$\frac{V_0}{Q} = \frac{-R_f s}{(R_f C_f s + 1)\left(R_i \left(C_p + C_s\right) s + 1\right)}. \tag{1}$$

where s is the Laplace variable; R_f and C_f are the feedback resistor and capacitor of the charge amplifier, respectively; R_i is the input resistance of the amplifier circuit; C_p is the blocked (clamped) capacitance of the piezoelectric sensor; and C_s is the cable and parasitic stray capacitance in parallel with C_p. The transfer function exhibits two poles at $\omega_1 = 1/(R_f C_f)$ and $\omega_2 = 1/[R_i(C_p + C_s)]$, and a flat-band gain of $1/C_f$. In the implemented circuit, $R_f = 2\,\mathrm{M\Omega}$ and $C_f = 200\,\mathrm{nF}$, giving a high-pass corner frequency of $\omega_1 \approx 2.5\,\mathrm{rad\,s^{-1}}$ (approximately 0.4 Hz), well below the frequency range of interest. Each actuator is driven by a Dual-Channel 300 V Amplifier (BD300). The controllers are digitally implemented on an NI cRIO-9039 FPGA with a 10 kHz sampling frequency, which also monitors and records performance signals. Data acquisition modules include NI9215 for charge amplifier outputs, NI9234 for acceleration measurements, and NI9264 for generating excitation signals for the shaker and piezoelectric actuators.

2.2. Mechatronic metamaterials architecture

Before describing the architecture, it is worthwhile to justify the use of the term *metamaterial* for the proposed design. Following the foundational criteria established by Liu et al (2000), and theoretically formalized for finite elastic structures by Hussein et al (2014), Sugino et al (2016), a locally resonant metamaterial must satisfy three conditions: (i) a periodic architecture with a repeating structural motif,

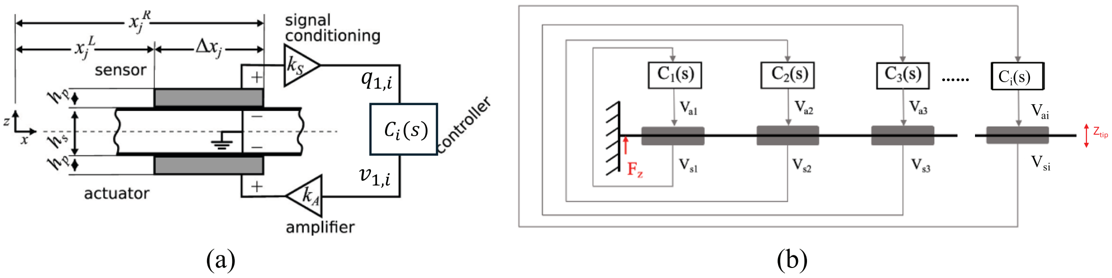

Figure 1. (a) Schematic representation of a single unit cell integrated with a collocated actuator–sensor configuration driven through the controller $C_i(s)$, and (b) representation of a metabeam with the ith unit cells distributed along its length (Kaczmarek *et al* 2024b).

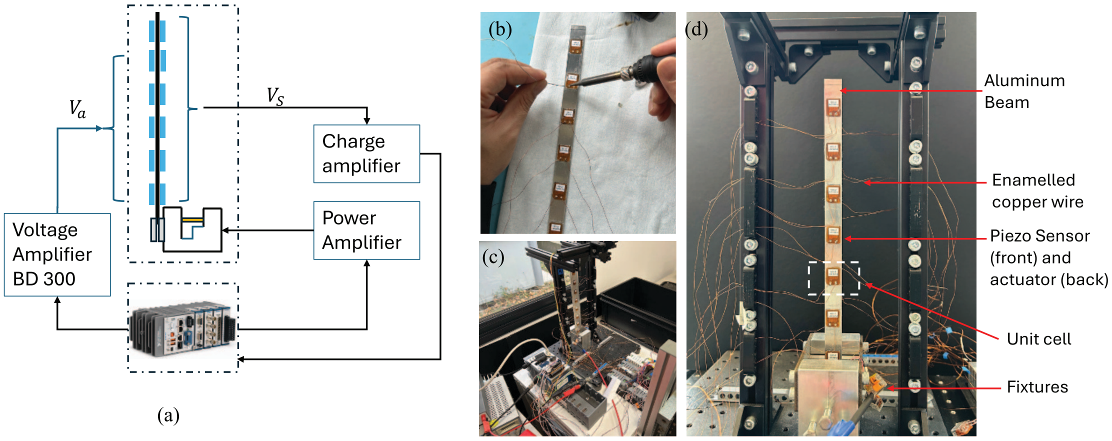

Figure 2. (a) Block diagram of the signal conditioning and actuation architecture, showing the charge amplifier, power amplifier, and voltage amplifier (BD300) connections for a single unit cell; (b) fabrication of the mechatronic metamaterial beam showing piezoelectric actuators and sensors attached to the front and back surfaces of the beam, and soldering of enameled copper wire connections; (c) close-up view of the assembled beam with unit cells, fixtures, and wiring; (d) complete experimental setup for closed-loop measurement, including the metabeam, signal conditioning electronics, FPGA controller, and testbed.

(ii) locally resonant units that introduce a frequency-dependent dynamic compliance at the unit-cell level, and (iii) an emergent bandgap arising from the collective action of these local resonators that cannot be attributed to Bragg scattering or any single unit cell in isolation. This design satisfies all three criteria. First, seven identical unit cells are periodically distributed along the host beam with uniform spacing, providing the required periodic motif. Second, each unit cell contains a collocated piezoelectric sensor–actuator pair governed by a resonant feedback controller that introduces a localized frequency-dependent dynamic compliance, functionally equivalent to an attached mechanical resonator in a passive locally resonant metamaterial. Third, the collective action of these digitally synthesized local resonators produces a frequency band of globally suppressed transmissibility that is sub-wavelength in character, confirmed by the fact that the inter-cell spacing is far smaller than the elastic wavelength at the bandgap frequencies of 20–100 Hz. The term *mechatronic* distinguishes this design from passive metamaterials: the local resonance is electronically synthesized through digital feedback rather than achieved through physical mass–spring attachments, consistent with the terminology adopted in Fang *et al* (2022), Kaczmarek and HosseinNia (2024).

The complete metamaterial architecture is generated once the beam is covered with N repeated collocated piezoelectric transducers along its length. In this configuration, all the piezoelectric patches are poled in the thickness direction. A visual representation of such a structure with n unit cells is shown in figure 1. Here, $i = 1, \ldots, n$ denotes the unit cell index, V_{si} is the voltage produced by the ith sensor, V_{ai} is the voltage sent to the ith actuator, and $C_i(s)$ denotes the controller implemented for unit cell i. Specifically, the patch sensor output is related to the average beam curvature at its location, whereas the actuator produces a pair of bending moments with amplitudes proportional to the applied voltage.

The transfer function from actuator 1 to sensor 7 is of primary interest for analyzing system transmissibility and characterizing vibrational bandgap formation. This is critical for identifying the attenuation frequency region and, consequently, characterizing bandgap performance. The actuator-sensor

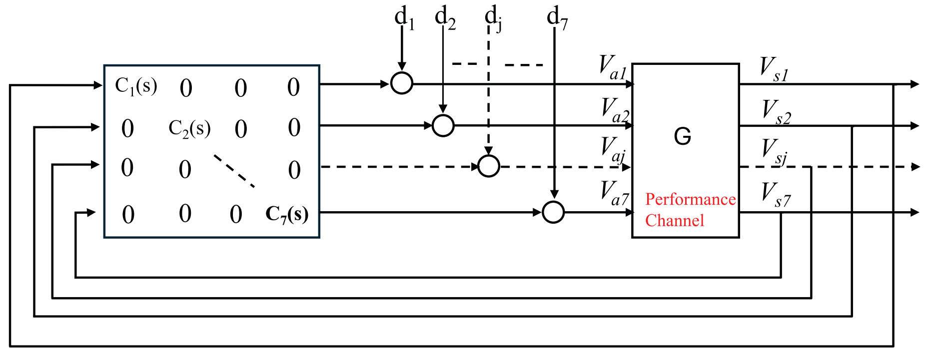

Figure 3. Closed-loop block diagram of the decentralized control architecture used in active piezoelectric metamaterials.

dynamics and their cross-coupling therefore define the performance channel within which bandgaps are targeted. The collocated channel is defined by the transfer function from actuator voltage V_{ai} to sensor voltage V_{si}. Controllers $C_i(s)$ are applied to these collocated channels with the objective of inducing bandgaps in the performance channel. The considered configuration of mechatronic metamaterial is shown figure 1.

2.3. Controller implementation

Active control for generating locally resonant bandgaps in beamlike piezoelectric metastructures requires: (1) a sensor to measure vibrations, (2) an actuator to suppress them, and (3) a control system to close the loop. Each unit cell forms an independent control loop acting as a local resonator. A decentralized control strategy is adopted, where each sensor-actuator pair operates independently, enhancing robustness and enabling parallel computation. Figure 3 illustrates the closed-loop block diagram. Controllers $C_i(s)$ aim to minimize the influence of base excitation F_z on tip displacement z_{tip}. The plant G represents the metastructure, and d_i denotes disturbances within each unit cell. The controller matrix is block-diagonal, reflecting the absence of inter-cell coupling. Given such control architecture, the controllers $C_i(s)$ are pivotal in defining the unit cell dynamics and generating a bandgap.

2.4. Analytical framework for $n \times n$ feedback design

To quantify the effect of local feedback on system behavior, we consider a general multivariable plant $G(s) \in \mathbb{R}^{n\times n}$, where each element $G_{ij}(s)$ represents the transfer function from actuator j to sensor i. The control architecture is decentralized, with a diagonal controller matrix:

$$C(s) = \text{diag}\left(C_1(s), C_2(s), \ldots, C_n(s)\right) \tag{2}$$

Each controller $C_i(s)$ is implemented as a second-order low-pass filter:

$$C_i(s) = \frac{g_i}{\dfrac{s^2}{\omega_c^2} + 2\zeta_{c_i}\dfrac{s}{\omega_c} + 1} \tag{3}$$

where:

- ω_c is the fixed resonant frequency where the bandgap is targeted,
- g_i and ζ_{c_i} are controller gain and damping, tuned individually per unit,
- The gains satisfy the condition $g_i < G_{ii}(0)^{-1}$ to ensure stability and passivity.

Each controller is tuned based solely on its corresponding local plant $G_{ii}(s)$. This allows modular tuning while accounting for minor variations due to non-ideal collocation or dynamics.

The closed-loop response of the system under external actuation is described by:

$$X(s) = \left(I + C(s)G(s)\right)^{-1} G(s)\, d(s) \tag{4}$$

where $d(s) \in \mathbb{R}^n$ is the vector of disturbance inputs and $X(s) \in \mathbb{R}^n$ is the vector of sensor outputs.

To evaluate vibration transmission, we apply excitation only at actuator 1 to emulate the base excitation scenario:

$$d(s) = [d_1(s), 0, \ldots, 0]^{\mathrm{T}} \tag{5}$$

yielding:

$$X(s) = d_1(s) \cdot (I + C(s)G(s))^{-1} G_{:,1}(s) \tag{6}$$

The use of actuator 1 as the excitation source is justified as follows. Since the transmissibility of interest is defined as the ratio $x_7(s)/x_1(s)$, the input type cancels in the ratio, meaning the measured transmissibility characterizes wave attenuation along the beam independently of whether excitation is applied via a base shaker or an internal piezoelectric bending moment, provided the response remains within the linear elastic regime. Furthermore, in a clamped-free beam, base excitation enters primarily through the root reaction moment, which is well-approximated by a concentrated bending moment near the clamped end that is precisely the actuation mechanism of actuator 1, located closest to the root. This approach also gives a cleaner input signal at low frequencies compared to shaker excitation, where mechanical noise and boundary coupling would reduce the sensor signal-to-noise ratio, and is consistent with the methodology of Kaczmarek and HosseinNia (2024).

2.4.1. Analytical expression for the transmissibility ratio

We partition $G(s)$ as:

$$G(s) = \begin{bmatrix} G_{11}(s) & g_{12}^{\top}(s) \\ g_{21}(s) & G_{22}(s) \end{bmatrix} \tag{7}$$

where $g_{12}(s), g_{21}(s) \in \mathbb{R}^{n-1}$ and $G_{22}(s) \in \mathbb{R}^{(n-1)\times(n-1)}$.

Since all unit cells are physically identical and instrumented with collocated piezoelectric sensor–actuator pairs of the same type, their local transfer functions $G_{ii}(s)$ share the same qualitative dynamic character, as confirmed by the experimentally measured collocated Bode plots in figure 6(a), where all seven responses overlap closely in shape. The primary cell-to-cell variation is a quantitative difference in low-frequency gain, which is fully absorbed into the individually tuned gains g_i satisfying $g_i < G_{ii}(0)^{-1}$. The assumption $C_i(s) = C(s)$ therefore applies only to the shared controller transfer function shape—the resonant frequency ω_c and damping ζ_c, while gain adaptation inherently compensates for spatial structural asymmetry. It is therefore reasonable to assume that all controllers share identical parameters, i.e.

$$C_i(s) = C(s), \quad \forall i = 1, \ldots, n. \tag{8}$$

This assumption simplifies the analysis while still accurately capturing the feedback behavior of the structure. It also reflects the practical implementation, where a single controller design is duplicated across all unit cells for ease of tuning and hardware uniformity.

For this identical-controller case, define

$$\eta(s) = (I_{n-1} + C(s)G_{22}(s))^{-1} g_{21}(s), \tag{9}$$

and let e_{n-1} be the unit vector in $\mathbb{R}^{n-1}$ selecting the last entry (corresponding to sensor n). The closed-form transmissibility ratio is

$$\frac{x_n(s)}{x_1(s)} = \frac{e_{n-1}^{\top}\eta(s)}{G_{11}(s) - C(s)g_{12}^{\top}(s)\eta(s)}. \tag{10}$$

This result follows from block elimination of the closed-loop equations and avoids forming the full inverse $(I + C(s)G(s))^{-1}$.

2.4.2. Experimental case: 7 × 7 unit cell

In the experimental setup, a flexible aluminum beam is instrumented with $n = 7$ collocated piezoelectric actuator-sensor pairs. The plant transfer matrix $G(s) \in \mathbb{R}^{7\times7}$ is identified through experimental frequency response measurements. Each diagonal term $G_{ii}(s)$ is used to independently tune $C_i(s)$, thereby implementing the decentralized control law described in section 2.3.

Once the controllers are implemented, a chirp signal is injected through actuator 1 while all controllers remain active. The measured output $X(s)$ is used to evaluate the transmissibility vector:

$$T(s) = (I + C(s)\,G(s))^{-1}\,G_{:,1}(s) \tag{11}$$

and each element is normalized by the first component to give:

$$\frac{x_k(s)}{x_1(s)} = \frac{T_k(s)}{T_1(s)}, \quad k = 2, \dots, 7. \tag{12}$$

For $n = 7$, write

$$\eta(s) = (I_6 + C(s)\,G_{22}(s))^{-1}\,g_{21}(s), \qquad e_6 = [0,0,0,0,0,1]^\top, \tag{13}$$

so that the end-to-end transmissibility is

$$\frac{x_7(s)}{x_1(s)} = \frac{e_6^\top \eta(s)}{G_{11}(s) - C(s)\,g_{12}^\top(s)\,\eta(s)}. \tag{14}$$

The expressions in (10) (and their 7 × 7 specialization above) provide analytic predictions for the measured transmissibility, which will be used to show the bandgap experimentally.

3. Experimental results and observed bandgaps

The identified MIMO plant is shown in figure 4, where only magnitude responses are presented for clarity. The system is represented by the transfer matrix $G(s)$, with inputs corresponding to actuator voltages $V_{a1}, \dots, V_{a7}$ (columns) and outputs corresponding to sensor signals $V_{s1}, \dots, V_{s7}$ (rows). Thus, each element $G_{ij}(s)$ denotes the transfer function from actuator V_{ai} to sensor V_{sj}; for instance, $G_{11}(s)$ represents the path from V_{a1} to V_{s1}, $G_{77}(s)$ from F_z to z_{tip}, and $G_{36}(s)$ from V_{a6} to V_{s3}.

The resonant dynamics are applied to each individual collocated unit cell following the rules described in the previous section 2.4.2, from equations (11)–(14). The physical rationale for using bending strain at the piezoelectric sensors as the unit-cell-level observable is as follows. The piezo-sensor charge is proportional to the local beam curvature at the patch location, making it directly sensitive to the moment-based phase cancellation that underlies resonant actuation. When the controller suppresses this local curvature, it effectively introduces a localized dynamic stiffness that impedes bending wave propagation past that unit cell. Tip displacement, by contrast, integrates contributions from all modes and hides this unit-cell-level physics. Bandgap formation is therefore physically understood through bending strain suppression at the unit-cell level, and quantitatively validated through the end-to-end closed-loop transmissibility from actuator 1 to sensor 7, computed analytically using equation (14) and measured experimentally, as shown in figures 5 and 7, confirming strong agreement between the derived analytical framework and the physical system response.

The corner frequency of the controller is tuned to lie in the vicinity of the desired bandgap region, and the control is implemented in the frequency domain, as illustrated in figure 6. Here, the controllers act as distributed virtual resonators coupled through the host beam dynamics. Each controller introduces a localized anti-resonance, and their combined action along the beam modifies the global transfer function, transforming isolated anti-resonance notches into a continuous frequency band of reduced transmissibility. This coordinated interaction among controlled unit cells is responsible for the emergence of bandgaps in the closed-loop system. Experimentally designed bandgaps at targeted frequencies, ranging from high to low, along with the influence of controller dynamics on the attenuation width, are shown in figure 7. The influence of the resonant controller progressively diminishes with decreasing frequency, as the active metabeam system inherently exhibits high-pass characteristics that directly affect bandgap formation, particularly its bandgap width. As a result, the attenuation associated with the bandgaps diminishes nonlinearly toward lower frequencies and displays a quasi-exponential decay trend in the response magnitude.

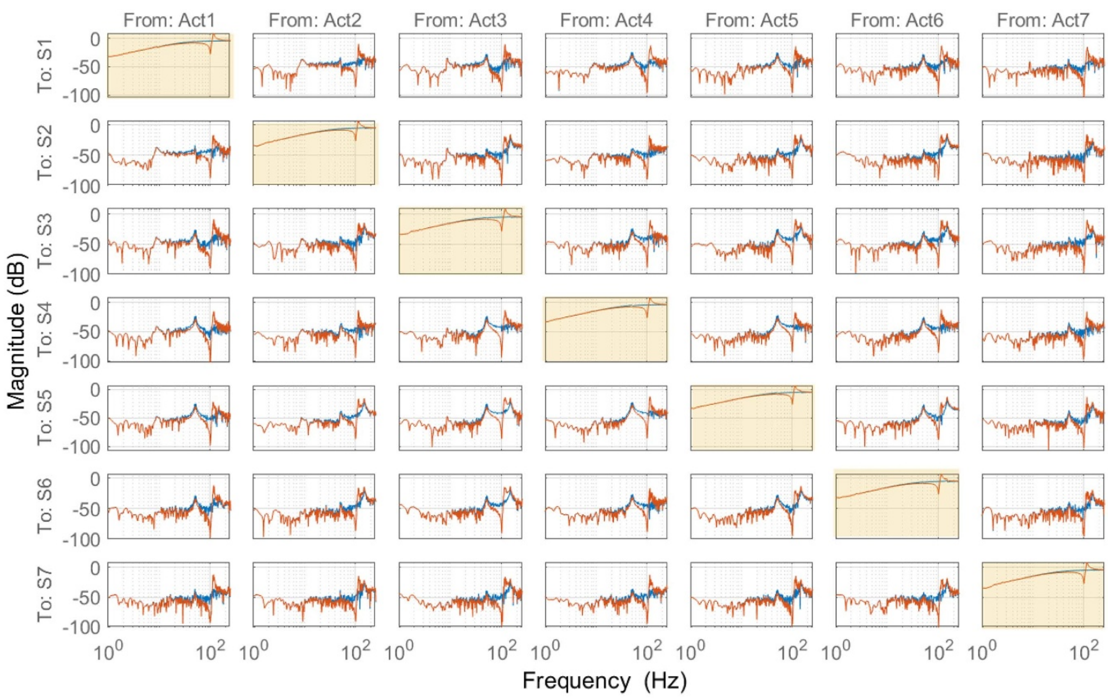

Figure 4. Experimental frequency response magnitudes of the full 7×7 plant $G(s)$, showing open-loop (blue) and simulated closed-loop responses (red) obtained by applying the resonant controller to all collocated sensor–actuator pairs. Each subplot $G_{ij}(s)$ represents the transfer function from actuator V_{ai} to sensor V_{sj}. The collocated responses $G_{ii}(s)$ are diagonally highlighted in yellow and are used individually to tune the decentralized controllers $C_i(s)$.

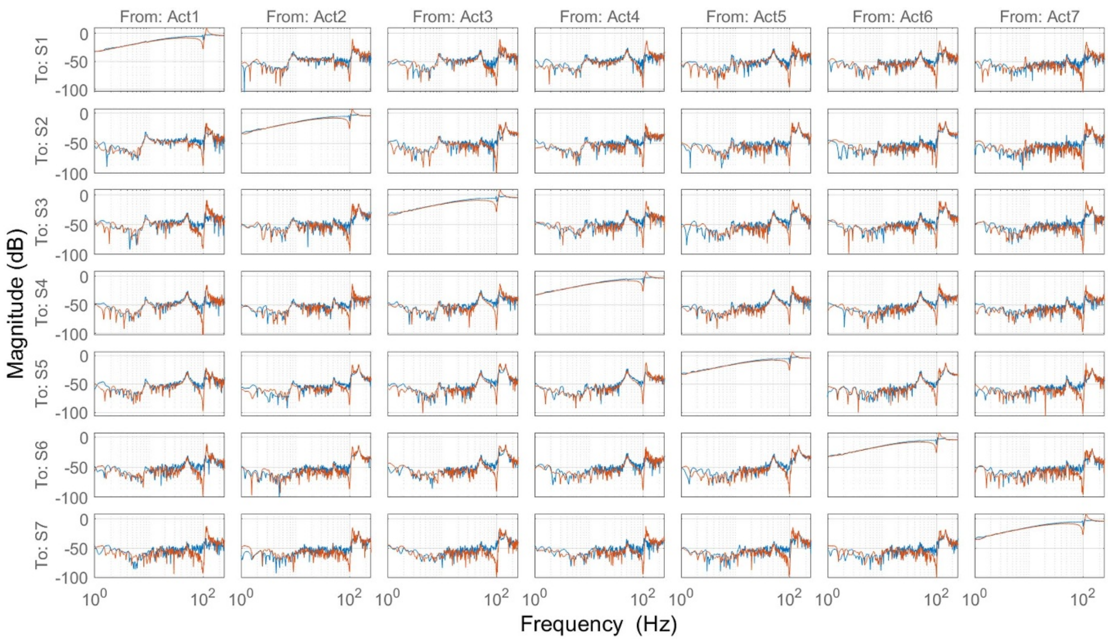

Figure 5. Experimental validation of the end-to-end closed-loop transmissibility from actuator 1 to sensor 7, comparing the experimentally measured closed-loop response (blue) with the analytical prediction from equation (14) (red). The residual peaks visible in the simulated response arise from lightly damped structural modes present in the identified plant $G(s)$; in the experimental closed-loop result, these narrow-band peaks are attenuated by the combined effect of controller damping and measurement noise averaging.

3.1. Effect of the controller gains and damping

The selection of controller gains in the second-order low-pass resonant filter with negative position feedback plays a crucial role in shaping the bandgap characteristics. High feedback gains increase the virtual stiffness and damping around the targeted resonant modes, leading to sharper and wider attenuation

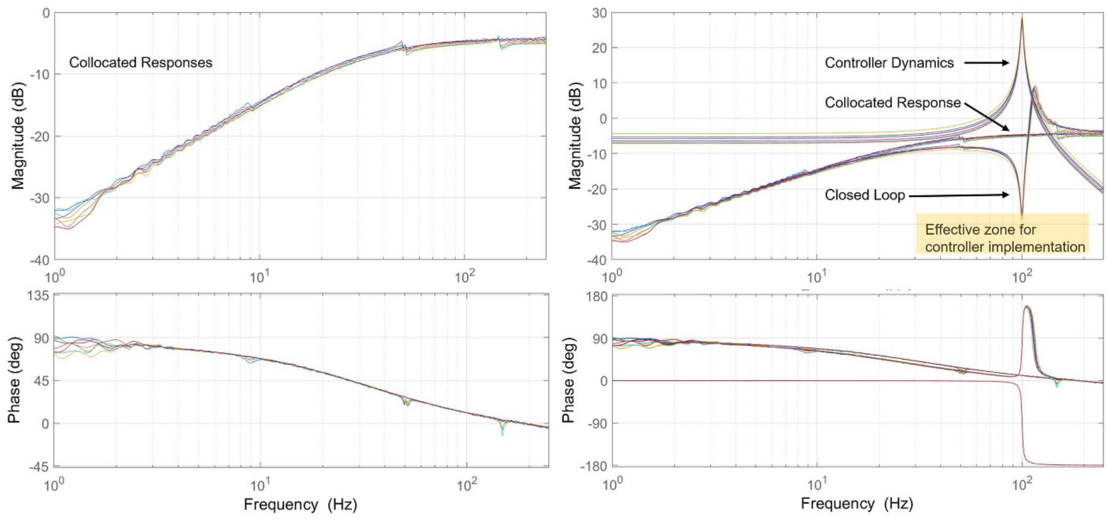

(a) (b)

Figure 6. Bode magnitude and phase responses of all collocated actuator–sensor transfer functions (a). The effect of second-order low-pass resonant filter with negative position feedback controllers implemented on the respective collocated transfer functions is also illustrated (b), demonstrating the achievable vibration attenuation and phase modification.

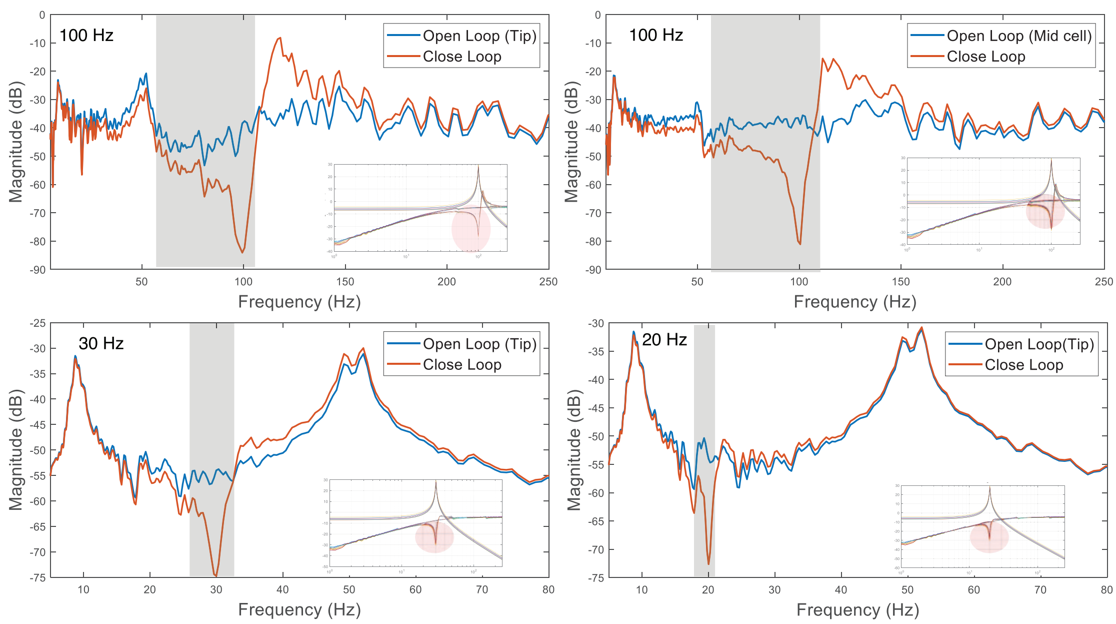

Figure 7. Experimentally designed vibration bandgaps at different frequencies. Responses without controller dynamics are shown in blue, and responses with the controller applied are shown in red.

zones in the frequency response. However, excessively high gains result in controller–structure interactions, introducing spillover or modal instability outside the intended frequency range, as shown in figure 8. The gain effect across different unit cells is directly influenced by the proximity of their dominant modal frequencies to the targeted corner frequency or bandgap. For example, when the targeted bandgap lies near the first modal frequency, applying a high control gain is effective primarily in the first unit cell, as shown in figure 8(a). Consequently, additional control effort or power input in the remaining cells becomes redundant, as depicted in figures 8(b) and (c). The same reasoning extends to higher frequency ranges, where only those unit cells whose modal frequencies lie close to the targeted bandgap region significantly contribute to the control performance.

The spatial distribution of mode shapes dictates how vibrational energy is localized along the structure. When the targeted frequency lies close to a particular mode, the associated deformation pattern dominates the system response. Unit cells located near the anti-nodes of that mode experience the largest bending strain and, therefore, interact most effectively with the control system. In contrast, unit cells

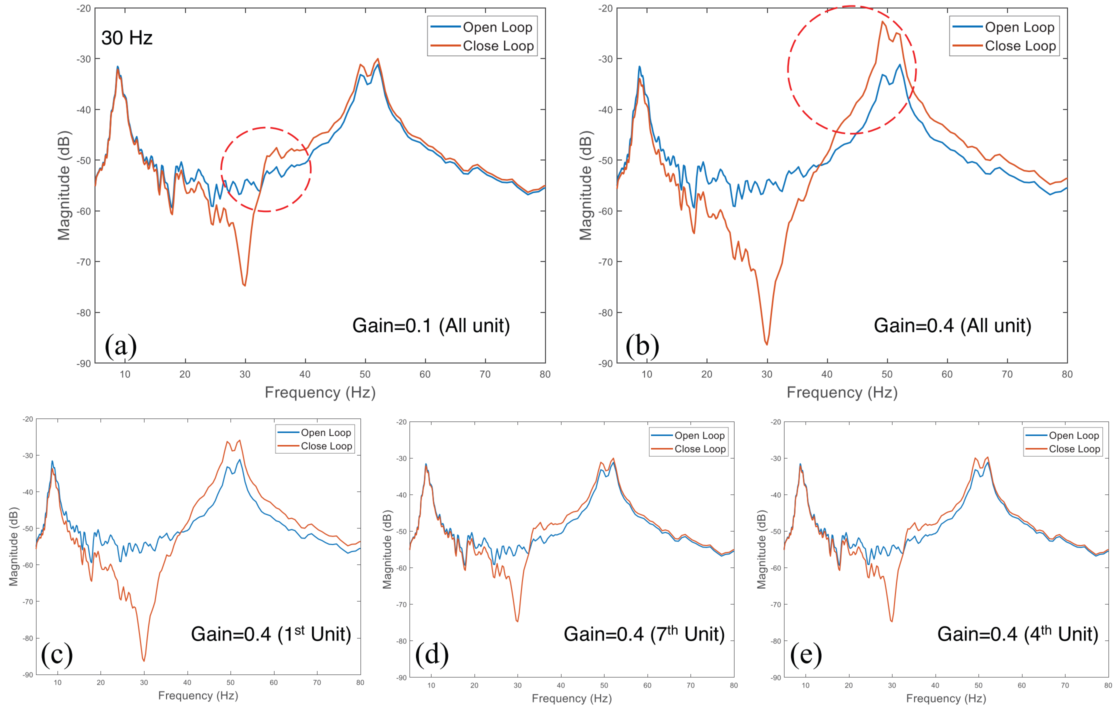

Figure 8. Effect of the controller gain on the low-frequency transmissibility response at a target frequency of 30 Hz. (a) Low gain ($g_i = 0.1$) applied to all unit cells; (b) high gain ($g_i = 0.4$) applied to all unit cells, showing a well-formed bandgap with control spillover (dashed red circle); (c) gain applied to the 1st unit cell only, demonstrating dominant contribution near the clamped root; (d) gain applied to the 7th unit cell only, showing negligible contribution near the free tip; (e) gain applied to the 4th (middle) unit cell only. Open-loop and closed-loop responses are shown in blue and orange, respectively.

near nodal regions contribute negligibly to the overall response, making additional control gain or transducer activation energetically inefficient. Consequently, for each targeted modal range, the effective number of active unit cells corresponds closely to the number of dominant modes participating in the dynamic response, which is consistent with the observations of Kaczmarek *et al* (2024a) for low-frequency bandgaps in cantilevers. The damping ratio, embedded in the controller's transfer function, directly influences the smoothness and depth of the attenuation band, affecting both amplitude suppression and transient behavior. Optimal damping must be tuned to suppress resonances effectively while avoiding excessive bandwidth overlap that can blur distinct bandgaps. Experimental observations from the piezo-distributed metabeam reveal that precise calibration of gain–damping pairs leads to localized modal suppression and shifts in peak transmissibility, providing a programmable mechanism for vibration rejection. Thus, controller design is not merely a stabilizing tool but a tunable parameter space that governs the effective dispersion relation and wave attenuation characteristics of the mechatronic metamaterial.

4. Discussion

The transmissibility ratio provides equation (10) a quantitative measure of how decentralized resonant controller with negative feedback modifies vibration transmission relative to the (uncontrolled) plant structural dynamics. Normalizing the closed-loop transmissibility

$$T_k^{\mathrm{cl}}(s) = \frac{e_{k-1}^T \eta}{G_{11} - C g_{12}^T \eta}, \qquad \eta = (I_6 + CG_{22})^{-1} g_{21},$$

by the scalar $e_{k-1}^T \eta$ yields

$$T_k^{\mathrm{cl}}(s) = \frac{1}{\alpha_k(s) - C(s)\beta_k(s)}, \qquad \alpha_k := \frac{G_{11}}{e_{k-1}^T \eta}, \qquad \beta_k := \frac{g_{12}^T \eta}{e_{k-1}^T \eta}.$$

This form shows that attenuation is governed by the magnitude of the effective denominator $D_k(s) := \alpha_k(s) - C(s)\beta_k(s)$, since small $|T_k^{\mathrm{cl}}|$ is equivalent to large $|D_k|$. Inter-cell coupling enters through G_{22}

in $\eta = (I_6 + CG_{22})^{-1} g_{21}$ and therefore directly shapes both α_k and β_k. In particular, stronger coupling modifies η such that the feedback-driven interaction ratio β_k is enhanced and/or becomes more favorably phased with the resonant controller $C(s)$ near the tuning frequency. As a result, $|D_k(j\omega)|$ increases over the targeted frequency interval, leading to reduced $|T_k^{\mathrm{cl}}(j\omega)|$ and stronger bandgap attenuation, as observed experimentally in the figures 6 and 8.

In summary, the closed-loop transmissibility provides a rigorous metric for evaluating the effectiveness of decentralized resonant feedback in suppressing vibration transmission. Reduced closed-loop transmissibility over targeted frequency intervals directly indicates the formation of active bandgaps, and confirms enhanced vibration isolation achieved through decentralized resonant control. Bandgaps are also influenced by the intrinsic capacitance C_{p} of the piezoelectric material. When combined with the feedback resistor R_{f} of the charge amplifier, this forms a high-pass network with corner frequency $\omega_{\mathrm{hp}} = 1/(R_{\mathrm{f}} C_{\mathrm{f}})$, as introduced in section 2.1.

It is important to distinguish the primary bandgap formation mechanism—the collective action of periodically distributed resonant controllers acting as virtual locally resonant oscillators, as described in sections 2.2 and 3—from the practical hardware consideration discussed below, which concerns the influence of the charge amplifier RC high-pass characteristics on the effective loop gain at low frequencies.

This HP behavior introduces a parasitic attenuation of the sensor signal at low frequencies, which must be compensated for if the controller is to remain effective in that range. The resonant dynamics of the controller are most effective when the collocated transfer function approaches the 0 dB line, where the characteristic dip appears, as shown in figure 6. We emphasize that this dip is a consequence of the HP roll-off acting on the underlying piezoelectric dynamics, rather than an independent attenuation mechanism; the controller compensates for the resulting signal loss rather than exploiting the HP behavior as a design feature.

At higher frequencies, where the HP effect is negligible, the collocated response exhibits a well-defined dip; at lower frequencies, however, this dip diminishes as the amplifier attenuation reduces the effective sensor signal available to the controller. To recover sufficient loop gain, higher controller gain values are applied at lower target frequencies. As a consequence, the controller corner frequency does not need to coincide with a structural resonance to achieve bandgap formation; the gain itself, rather than proximity to a structural mode, is what restores sufficient attenuation at the targeted frequency. The combined action of multiple resonant controllers distributed along the structure then produces a targeted bandgap over a wide range of frequencies.

To incorporate the RC high-pass characteristics into the analytical framework, we consider the charge amplifier transfer function given in equation (1). At low frequencies, the amplifier output is attenuated by the high-pass filter with corner frequency $\omega_{\mathrm{hp}} = 1/(R_{\mathrm{f}} C_{\mathrm{f}})$. This modifies the effective collocated transfer function seen by the controller. Specifically, the measured sensor voltage V_{si} is not the true piezoelectric charge signal Q_i, but rather its high-pass filtered version:

$$V_{si}(s) = H_{\mathrm{hp}}(s) \cdot \frac{Q_i(s)}{C_{\mathrm{f}}}, \qquad H_{\mathrm{hp}}(s) = \frac{-R_{\mathrm{f}} C_{\mathrm{f}} s}{R_{\mathrm{f}} C_{\mathrm{f}} s + 1} \tag{15}$$

This introduces a frequency-dependent attenuation of the sensor signal below ω_{hp}, which directly reduces the effective loop gain $|G_{ii}(j\omega) C_i(j\omega)|$ at low frequencies. The effective collocated transfer function as seen by the controller therefore becomes:

$$\tilde{G}_{ii}(s) = H_{\mathrm{hp}}(s) \cdot G_{ii}(s). \tag{16}$$

The bandgap existence condition $g_i < \tilde{G}_{ii}(0)^{-1}$ must consequently be re-evaluated in terms of $\tilde{G}_{ii}$ rather than G_{ii}. Since $|H_{\mathrm{hp}}(j\omega)| \to 0$ as $\omega \to 0$, the effective DC gain $\tilde{G}_{ii}(0) \to 0$, which means the stability margin $g_i < \tilde{G}_{ii}(0)^{-1}$ is automatically satisfied at sufficiently low frequencies. However, the reduced loop gain also means that higher controller gains g_i are required to restore sufficient attenuation depth in the collocated response, which explains the quasi-exponential decay of bandgap depth observed at lower target frequencies in figure 7.

The characteristic dip visible in the low-frequency collocated response (figure 6) is a direct manifestation of this HP effect: the magnitude rolls off below ω_{hp} and approaches the 0 dB line only at frequencies where the piezoelectric coupling dominates over the amplifier attenuation. The resonant controller is most effective precisely at this crossover, where the collocated response approaches 0 dB and a deep anti-resonance dip can be induced.

This analysis provides a practical design rule: the controller corner frequency ω_{c} should be placed where $|\tilde{G}_{ii}(j\omega_{\mathrm{c}})| \approx 0$ dB, since this is where the gain required to compensate for HP-induced signal loss is minimized for a given target attenuation depth. This rule remains valid even when no structural resonance is present at that frequency, since the relevant compensation is for amplifier roll-off, not for proximity to a structural mode.

5. Conclusion

The main findings of this study can be summarized as follows:

- We experimentally demonstrated digitally controlled mechatronic metamaterials with collocated piezoelectric sensor–actuator pairs, showing that second-order low-pass resonant filters with negative position feedback can successfully generate targeted vibration bandgaps, including in low-frequency regions where passive methods are fundamentally limited.
- The effectiveness of the resonant controller was confirmed through systematic tuning of gain, damping, and resonance frequency, enabling programmable and frequency-selective attenuation zones along the metabeam.
- Analytical and experimental results show strong agreement. The derived closed-loop transmissibility framework provides a rigorous theoretical basis that matches experimental observations and offers a practical tool for shaping and interpreting bandgap behavior by explicitly accounting for inter-cell coupling and localized dynamic effects. This framework further serves as a predictive tool for active bandgap design, as reduced closed-loop transmissibility over targeted frequency intervals directly explains the emergence of active bandgaps and the enhancement of vibration isolation achieved through decentralized resonant control.
- Bandgap formation was shown to be achievable through controller-induced virtual resonator dynamics even when the controller corner frequency does not coincide with a structural resonance, provided the controller gain is sufficient to compensate for the high-pass roll-off of the charge amplifier at low frequencies. This finding opens new pathways toward adaptive control strategies, multi-dimensional grading, and reconfigurable metamaterial architectures capable of real-time wave manipulation.

Several directions are identified for future investigation. Time-domain transient analysis of the controlled metabeam, including the evolution of amplitude and phase distribution across unit cells under impulsive excitations, would provide complementary insight beyond the frequency-domain characterization presented here. Additionally, spatially graded controller designs that individually optimize ω_c and ζ_c per unit cell could more effectively enhance bandgap width and mitigate control spillover at higher gains. Finally, extension of the present $n \times n$ framework to two-dimensional plate structures represents a promising pathway toward fully programmable mechatronic metamaterial platforms for broadband vibration isolation.

Acknowledgments

This work was supported by the Netherlands Organization for Scientific Research (NWO) under the HTSM Applied and Technical Science Program, project *MetaMech*, grant number 17976. The authors acknowledge ASML Veldhoven for the use-case motivation provided within the project.

Data availability statement

All data that support the findings of this study are included within the article (and any supplementary files).

Author contributions

Vivek Gupta 0000-0003-2790-2787
Conceptualization (lead), Data curation (lead), Formal analysis (lead), Investigation (lead), Methodology (lead), Resources (lead), Software (lead), Supervision (lead), Validation (lead), Visualization (lead), Writing – original draft (lead), Writing – review & editing (lead)

Aditya Natu 0009-0007-7676-8525
Data curation (supporting), Investigation (supporting), Validation (supporting)

S Hassan HosseinNia 0000-0002-7475-4628
Conceptualization (equal), Funding acquisition (lead), Methodology (equal), Project administration (lead), Supervision (equal), Writing – original draft (supporting), Writing – review & editing (supporting)

References

Das A, Bera K K and Banerjee A 2025 Wave propagation in thin-walled mono-symmetric metabeam with periodically placed piezoelectric sensor and actuator *Phys. Lett. A* **539** 130607

Failla G, Marzani A, Palermo A, Russillo A F and Colquitt D 2024 Current developments in elastic and acoustic metamaterials science *Phil. Trans. A* **382** 20230369

Fang W, Han C, Chen Y and Liu Y 2022 Valley hall elastic edge states in locally resonant metamaterials *Materials* **15** 1491

Gupta V, Adhikari S and Bhattacharya B 2020 Exploring the dynamics of hourglass shaped lattice metastructures *Sci. Rep.* **10** 20943

Gupta V, Munian R K and Bhattacharya B 2022 Dispersion analysis of the hourglass-shaped periodic shell lattice structure *Int. J. Solids Struct.* **254** 111931

Huang H H, Lin C K and Tan K T 2016 Attenuation of transverse waves by using a metamaterial beam with lateral local resonators *Smart Mater. Struct.* **25** 085027

Huang H and Sun C 2009 Wave attenuation mechanism in an acoustic metamaterial with negative effective mass density *New J. Phys.* **11** 013003

Hussein M I, Leamy M J and Ruzzene M 2014 Dynamics of phononic materials and structures: historical origins, recent progress and future outlook *Appl. Mech. Rev.* **66** 040802

Kaczmarek M B, Gupta V and HosseinNia S H 2024a Active piezoelectric metastructures: relationship of bandgap formation with unit cell number and modal behaviour *ASME Int. Mechanical Engineering Congress and Exposition* (American Society of Mechanical Engineers) p V001T01A001

Kaczmarek M B, Gupta V and HosseinNia S H 2024b Bandgap modulation in active metamaterial beams through feedback control *2024 Eighteenth Int. Congress on Artificial Materials for Novel Wave Phenomena (Metamaterials)* (IEEE) pp 1–3

Kaczmarek M B and HosseinNia S H 2024 Creating bandgaps in active piezoelectric slender beams through positive position feedback control *Smart Mater. Struct.* **33** 125039

Lin Z and Tol S 2023 Electroelastic metasurface with resonant piezoelectric shunts for tunable wavefront control *J. Phys. D: Appl. Phys.* **56** 164001

Liu Z, Zhang X, Mao Y, Zhu Y Y, Yang Z, Chan C T and Sheng P 2000 Locally resonant sonic materials *Science* **289** 1734–6

Nima Mahmoodi S, Ahmadian M and Inman D J 2010 Adaptive modified positive position feedback for active vibration control of structures *J. Intell. Mater. Syst. Struct.* **21** 571–80

Sugino C, Leadenham S, Ruzzene M and Erturk A 2016 On the mechanism of bandgap formation in locally resonant finite elastic metamaterials *J. Appl. Phys.* **120** 134501

Sugino C, Xia Y, Leadenham S, Ruzzene M and Erturk A 2017 A general theory for bandgap estimation in locally resonant metastructures *J. Sound Vib.* **406** 104–23

Wen S, Xiong Y, Hao S, Li F and Zhang C 2020 Enhanced band-gap properties of an acoustic metamaterial beam with periodically variable cross-sections *Int. J. Mech. Sci.* **166** 105229

Wu Z, Zhu B, Wang R and Zhang X 2022 Design of mechanical metamaterial for energy absorption using a beam with a variable cross-section *Mech. Mach. Theory* **176** 105027

Yuan Y, Zhou W, Li J, Chen W and Bao R H 2019 Tuning bandgaps in metastructured beams: numerical and experimental study *J. Zhejiang Univ. Sci. A* **20** 811–22

Zhu R, Liu X, Hu G, Sun C T and Huang G 2014 Negative refraction of elastic waves at the deep-subwavelength scale in a single-phase metamaterial *Nat. Commun.* **5** 5510